Design of Stable and Uniform Single Nanoparticle Photonics for *In Vivo* Dynamics Imaging of Nanoenvironments of Zebrafish Embryonic Fluids

Prakash D. Nallathamby, Kerry J. Lee, and Xiao-Hong Nancy Xu*

Department of Chemistry and Biochemistry, Old Dominion University, Norfolk, Virginia 23529

ARTICLE

ABSTRACT We report here the use of a simple washing approach to reduce the ionic strength of the solution, which increased the thickness of the electric double layer on the surface of silver (Ag) nanoparticles and thereby enhanced their surface ζ-potential. This approach allowed us to prepare optically uniform (75−99%) and purified Ag nanoparticles (11.3 ± 2.3 nm) that are stable (nonaggregation) in solution for months, permitting them to become robust and widely used single nanoprobes for *in vivo* optical imaging. These Ag nanoparticles show remarkable photostability and serve as single nanoparticle photonic probes for continuous imaging nanoenvironments of segmentation-stage zebrafish embryos for hours. Unlike other particle tracking experiments, we utilized size-dependent localized surface plasmon resonance spectra (LSPRS) (colors) of single Ag nanoparticles to determine given colored (sized) nanoparticles *in situ* and used the monodisperse color (size) of nanoparticles to simultaneously measure viscosities and flow patterns of multiple proximal nanoenvironments in segmentation-stage zebrafish embryos in real time. We found new interesting counterclockwise flow patterns with rates ranging from 0.06 to 1.8 μm/s and stunningly high viscosity gradients spanning two orders of magnitude in chorion space of the embryos, with the highest viscosity observed around the center of chorion space and the lower viscosity at the interfacial areas near the surface of both chorion layers and inner mass of the embryos. This study demonstrates the possibility of using individual monodisperse nanophotonics to probe the roles of embryonic fluid dynamics in embryonic development.

KEYWORDS: single nanoparticle photonics · single nanoparticle optics · silver nanoparticles · embryonic fluid dynamics · *in vivo* imaging · zebrafish embryos

Recent advances in nanoscience and nanotechnology suggest a wide variety of potential applications of nanoparticles, such as nanosensors[1−5] and nanophotonic probes for *in vivo* imaging, diagnosis, and smart drug delivery.[2,6−13] Silver nanoparticles exhibit the highest quantum yield (QY) of Rayleigh scattering among noble metal nanoparticles[14−16] and can be directly observed and characterized using dark-field single nanoparticle optical microscopy and spectroscopy (SNOMS).[1,5,6,9,10,17] Silver nanoparticles show the dependence of LSPR spectra on their size, shape, surrounding environment, and dielectric constant of the embedding medium.[14−16] By synthesizing uniform shape nanoparticles and dispersing them in the same dielectric constant of medium, we have used the color (LSPR spectra) index of Ag nanoparticles as a nanometer-size index to directly image single living cells and embryos at nanometer resolution in real time.[1,6,9,10,17] Unlike fluorescent probes, Ag nanoparticles resist photodecomposition and can serve as photostable nanoparticle probes to continuously monitor dynamics events of interest for an extended period of time.[1,6,9,10,17]

Silver nanoparticles could enter zebrafish embryos and exhibited dose-dependent toxicity on embryonic development, demonstrating the possibility of using low-dose Ag nanparticles as biocompatible nanoparticle probes for *in vivo* imaging.[6]

However, unlike gold nanoparticles, it is much more challenging to prepare monodisperse and stable (not aggregated) Ag nanoparticles that can be stored for a long period of time (months), which limits their potential applications as single nanophotonic probes for *in vivo* imaging. If the nanoparticle solution is stable only for days, one will have to resynthesize and recharacterize nanoparticles, which is time-consuming and expensive. It is especially problematic for biological experiments that need days and weeks to complete. Furthermore, it is essential that nanoparticles possess the superior stability for months, in order for them to become popular and robust probes, and be accessible to a wide spectrum of users. In fact, the stability of nanoparticles has been a primary obstacle for achieving a wide variety of applications of nanoparticle probes. Currently, an array of surface passivating agents, such as alkanethiol, 11-mercaptoundecanoic acid (MUA), and

*Address correspondence to xhxu@odu.edu.

Received for review January 25, 2008 and accepted June 02, 2008.

Published online June 11, 2008.
10.1021/nn800048x CCC: $40.75

polymers, have been used to functionalize nanoparticles, aiming to maintain the surface stability of nanoparticles and to prevent the nanoparticles from aggregation in solution.[1,18–23] However, the passivating agents change the intrinsic surface properties of nanoparticles, prohibiting investigation of their intrinsic optical properties and hindering the rational design of desired optical properties of single nanoparticle photonics. Some passivating agents also interfere with the study of *in vivo* systems of interest. Therefore, solving such a technical challenge is highly desirable and significant.

Zebrafish (*Danio rerio*) has become an emerging important vertebrate model system for drug discovery, better understanding of human diseases, and addressing an array of fundamental questions of development biology, such as determining the normal development of the left−right asymmetry in vertebrates.[24–28] Zebrafish embryos are transparent and develop outside of their mothers, and embryonic development is completed within 120 h postfertilization (hpf) with well-characterized development stages.[28–30] These features allow us to directly image embryonic fluid dynamics and early development of embryos simultaneously, offering the possibility of better understanding the role of the embryonic fluid dynamics in the early development of embryos. During embryogenesis, the embryonic stem cells divide and differentiate into the various cell lineages that constitute the tissue of different parts of the organism.[31–33] One of the determining factors of cell differentiation into different lineages is the nanoenvironments surrounding the cells.[34,35] Viscosity and flow patterns surrounding the cells in the embryonic fluids affect directions of movements of signaling molecules and migration of cells, which control embryonic morphogenesis, underscoring the importance of probing the viscosity gradients and flow patterns of embryonic fluid *in vivo* at nanometer resolution in real time. Unfortunately, no effective tools are currently available for mapping viscosity gradients and flow patterns of embryonic fluids *in vivo* at nanometer resolution in real time.

Particle tracking has been widely used to investigate the dynamics of molecules and their surrounding media *in vitro* and *in vivo*.[32,34,36–39] However, many of the particles used in the reported studies were large particles with diameters greater than 40 nm, and some had micrometer diameters, which diffused slowly and hence offered limited temporal and spatial resolution in determining dynamic events of interest *in vivo*. The reported studies did not investigate the effect of particle sizes on their measurements and were unable to determine the particle sizes *in situ* and in real time.[32,34,36–39] Thus, they could not select identical sized particles to simultaneously investigate several dynamic events of interest *in vivo* in real time.

In our previous study, we focused on probing the entry of nanoparticles into zebrafish embryos and investigating dose-dependent toxicity of Ag nanoparticles on embryonic development.[6] In this study, we further developed a simple washing step to prepare uniform Ag nanoparticles that were stable in solution for months and used them as single nanoparticle photonics to simultaneously probe several proximal nanoenvironments in segmentation-stage zebrafish embryos at nanometer resolution in real time, aiming to map embryonic fluid dynamics to better understand their roles in embryonic development and to develop stable and powerful nanophotonic probes for *in vivo* dynamics imaging at nanometer resolution in real time.

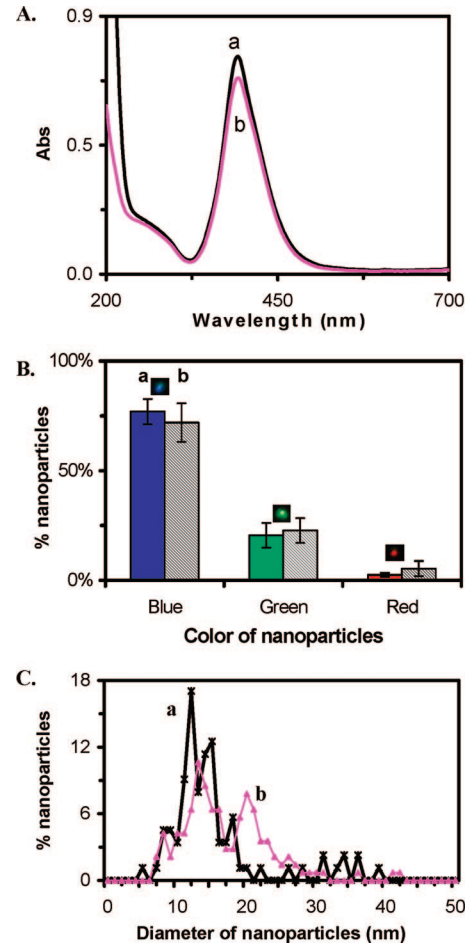

Figure 1. Characterization of stability and optical properties of unwashed Ag nanoparticles: (a) immediately and (b) at 2 months, after synthesis, respectively. (A) UV−vis spectra of 1.04 nM Ag nanoparticles show absorbance of (a) 0.76 and (b) 0.69 at 392 nm. (B) Histograms show distribution of colors of single nanoparticles acquired by SNOMS: (a) (77 ± 6)% blue, (21 ± 6)% green, and (2 ± 1)% red and (b) (72 ± 9)% blue, (23 ± 6)% green, and (5 ± 3)% red. (C) Histograms of size distribution of single nanoparticles measured by HRTEM show (a) 11.6 ± 2.4 nm and (b) 16.4 ± 6.3 nm.

RESULTS AND DISCUSSION

Synthesis and Characterization of the Stability of Ag Nanoparticles. The Ag nanoparticle solution was synthesized by reducing $AgClO_4$ with $NaBH_4$ and sodium citrate, as described in Methods. To investigate the stabil-

ity of the nanoparticles, we characterized their concentration, size, and optical properties in solution over 2 months after synthesis using UV−vis spectroscopy, SNOMS, high-resolution transmission electron microscopy (HRTEM), and dynamic light scattering (DLS), as shown in Figure 1. The UV−vis absorption spectrum of the Ag nanoparticles immediately after synthesis shows an absorbance of 0.76 with peak wavelength at 392 nm and a peak width at half-maximum (fwhm) of 63 nm (Figure 1A,a), indicating a narrow size distribution. The color (LSPRS) distribution of individual Ag nanoparticles determined using SNOMS shows that the solution consists of 77% blue, 21% green, and 2% red nanoparticles (Figure 1B,a). A histogram of the size distribution of individual Ag nanoparticles measured by HRTEM (Figure 1C,a) shows that the average size of nanoparticles is 10.7 ± 2.4 nm and their shape is spherical.[1]

We found that absorbance of the UV−vis spectrum began to decrease within 24 h after synthesis. By the end of 2 months, the peak absorbance decreased to 0.69 from an initial value of 0.76 with a slightly wider fwhm of 66 nm (Figure 1A,b). The histogram of the color distribution of individual nanoparticles (Figure 1B,b) shows 72% blue, 23% green, and 5% red nanoparticles, suggesting more green and red nanoparticles were generated in the solution over 2 months of storage. Histograms of size distribution measured by HRTEM (Figure 1C,b) illustrate an increase in size and distribution from 10.7 ± 2.4 to 16.4 ± 6.3 nm. Thus, the results in Figure 1 show that the unwashed nanoparticles were unstable and became less monodisperse over time.

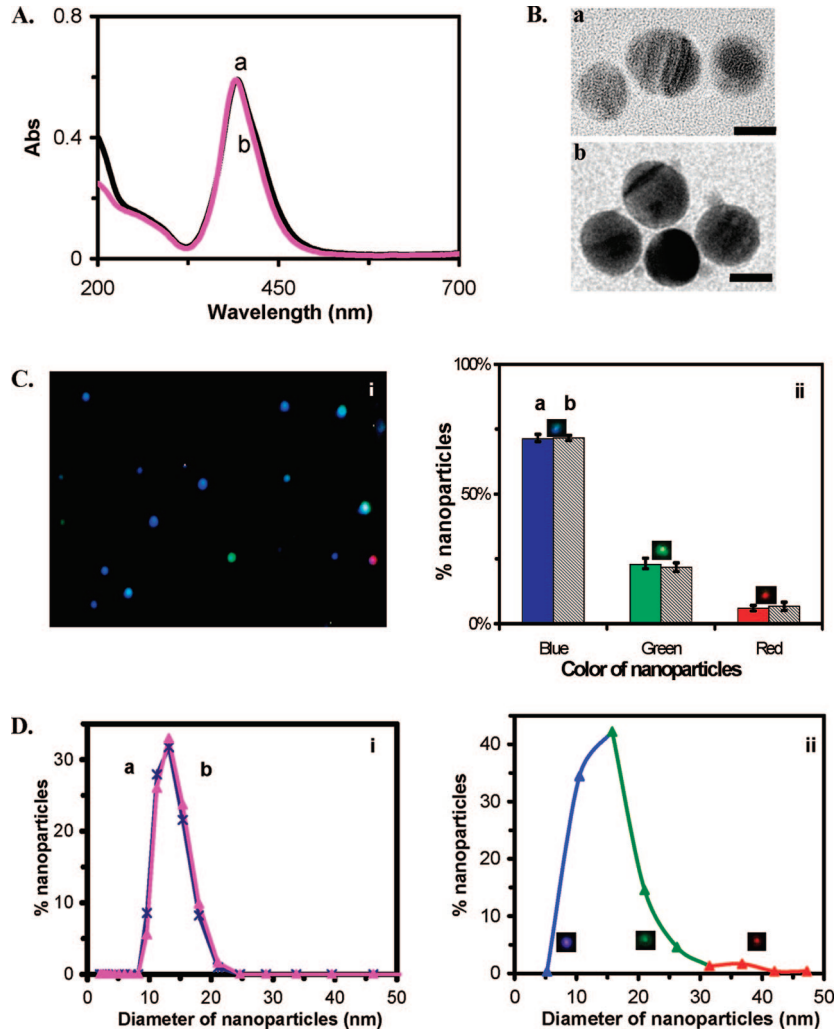

Figure 2. Characterization of stability and optical properties of washed Ag nanoparticles: (a) immediately and (b) at 2 months, after synthesis, respectively. (A) UV−vis spectra of 0.61 nM Ag nanoparticles show absorbance of (a and b) 0.59 at 392 nm. (B) HRTEM images show nearly uniform spherical nanoparticles. The scale bars are 10 nm. (C) Representative (i) dark-field optical image of single nanoparticles, and (ii) histograms show distribution of colors of single nanoparticles acquired by SNOMS: (a) (74 ± 6)% blue, (21 ± 4)% green, and (5 ± 3)% red; (b) (74 ± 5)% blue, (20 ± 4)% green, and (6 ± 1)% red. (D) Histograms of size distribution of single nanoparticles at (i) (13.2 ± 2.8) nm and (ii) (11.3 ± 2.3) nm measured by (i) DLS and (ii) HRTEM. In (ii), histogram also shows the correlation of colors with sizes of individual nanoparticles: 74% nanoparticles are blue (5−15 nm), 20% nanoparticles are green (16−33 nm), and 6% nanoparticles are red (34−45 nm).

To investigate the effect of the presence of reaction agents on stability and optical properties of single nanoparticles, once we completed the synthesis of nanoparticles, we immediately removed chemicals (*e.g.*, excess reagents and byproducts) involved in synthesis and washed the nanoparticles twice with nanopure water using centrifugation. We resuspended the nanoparticles in nanopure water and characterized their physical and optical properties. Interestingly, we found that the washed nanoparticles were much more stable than unwashed nanoparticles, and their physical and optical properties remained nearly constant over a period of at least 2 months (Figure 2). We found that the ζ-potential of the nanoparticles decreased from −19.96 to −35 mV after washing, showing an increase in surface charge and consequently higher stability of nanoparticles in solution. One plausible explanation is that, by removing chemicals from the nanoparticle solution, we decreased the ionic strength of the solution, which increased the thickness of electrical double layer on the surface of nanoparticles and enhanced the ζ-potential and surface charge of the nanoparticles. Thus, washed nanoparticles are more stable in solution than unwashed nanoparticles and can be stored for months.

The UV−vis spectra of the washed nanoparticles show an absorbance of 0.59 with peak wavelength at 392 nm and fwhm of 62 nm, which remained constant over 2 months (Figure 2A). HRTEM images show that the spherical shape of the nanoparticles also remained unchanged over 2 months (Figure 2B). Representative

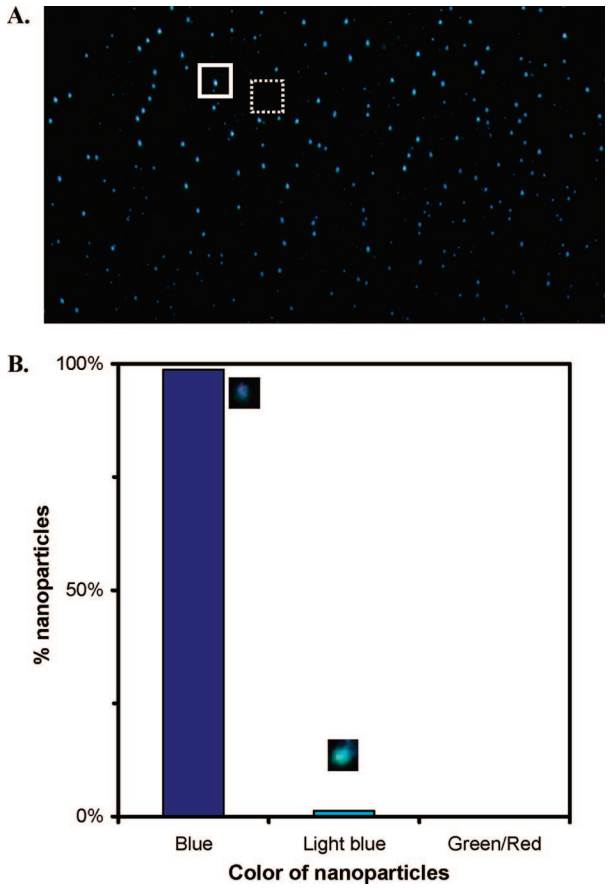

Figure 3. Characterization of optically uniform Ag nanoparticles: (A) representative optical image of individual Ag nanoparticles show uniform blue color; (B) histogram shows that 99% nanoparticles are blue with 1% light blue and no occurrence of green and red. The dashed line and solid line squares illustrate the representative detection areas for measuring the integrated intensity of the absence (background) and presence of individual nanoparticles (Figure 4), respectively, as described in Methods.

optical images and histograms of color distribution of single nanoparticles over 2 months illustrate that the majority (74%) of nanoparticles was blue with 21% green and 5% red (Figure 2C) and remained essentially the same over 2 months. Histograms of size distribution of nanoparticles in solution determined using DLS and HRTEM show that the average size of the nanoparticles was 13.2 ± 2.8 and 11.3 ± 2.3 nm, respectively, and remained unchanged over 2 months. Note that the hydrodynamic radii of nanoparticles in solution measured by DLS are always larger than those that are dried and measured using TEM because nanoparticles are hydrated in solution. That is why we observed the slightly larger radii of nanoparticles using DLS than using HRTEM.

We correlated the histogram of size distribution determined by HRTEM with the histogram of color (LSPRS) distribution of single nanoparticles characterized by SNOMS. The size distribution shows that 74% nanoparticles are 5−15 nm in diameter, 20% nanoparticles are 16−33 nm, and 6% nanoparticles are 34−45 nm. The color distribution exhibits that 74% nanoparicles are blue, 20% nanoparticles are green, and 6% of nanoparticles are red. Thus, we can correlate the color index of Ag nanoparicles as nanometer size index. This approach allows us to effectively use color (LSPRS) of individual nanoparticles to determine their sizes in solution at nanometer resolution using SNOMS. Note that, despite numerous studies,[14–16] currently it is still impossible to accurately compute and describe the LSPRS of individual given nanoparticles prepared by chemical synthesis because it appears that the surface morphologies and adsorbates of nanoparticles and surrounding medium play an important role in the optical properties of nanoparticles.[40] Our experimental approach of correlating size distribution with color (LSPRS) distribution is based on statistics and calibration approaches, which accurately reflects the size and color distribution at single nanoparticle resolution.

By carefully tuning the conditions of synthesis and washing of nanoparticles as described in Methods, we prepared nearly monodisperse single nanoparticle optics, showing that all nanoparticles are blue (99% blue and 1% light blue) (Figure 3). Blue nanoparticles are smaller nanoparticles (5−15 nm). Thus, they have lower QY of Rayleigh scattering and are less sensitively detected than green and red nanoparticles. Nevertheless, blue nanoparticles can be directly observed and characterized using SNOMS.

Characterization of Photostability of Single Nanoparticle Photonic Probes. We characterized the photostability of single nanoparticles by acquiring sequential optical images of single Ag nanoparticles while these nanoparticles were constantly radiated under a dark-field microscope illuminator (100 W halogen) for 12 h. The illumination power on the focal plane of dark field (the sample stage) measured by a power meter was (0.070 ± 0.001) W. The LSPR spectra of single nanoparticles before and after the 12 h illumination showed that the spectra remained unchanged (Figure 4A). Plots of scattering intensity of single nanoparticles and background (in the absence of nanoparticles) *versus* illumination time in Figure 4B show that the scattering intensity of individual single nanoparticles remains unchanged over 12 h. Zoom-in plots of Figure 4B with short frame interval of 40.6 ms (ms) further illustrate that small fluctuations of scattering intensity of single nanoparticles (Figure 4B&C: i) are similar to the intensity fluctuation of the background (Figure 4B&C: ii), showing that the intensity fluctuations are attributable to the illuminator and the noise level of CCD camera. Thus, the result in Figure 4 demonstrates that single Ag nanoparticles resist photodecomposition and blinking.

Characterization of Size-Dependent Diffusion of Single Nanoparticles. We then characterized the diffusion of single nanoparticles in solution and determined their dependence upon the size of nanoparticles using SNOMS. Unique features of single nanoparticle optics al-

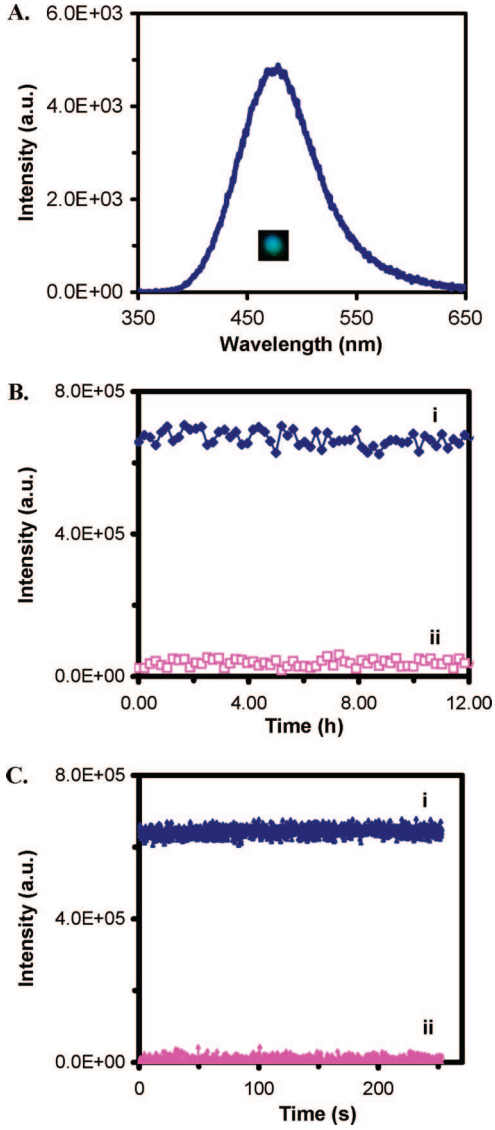

Figure 4. Characterization of photostability of individual Ag nanoparticles. (A) Representative LSPR spectrum (color) of a single Ag nanoparticle shows a peak wavelength at 476 nm. (B) Representative plots of scattering intensity of (i) a single nanoparticle and (ii) background *versus* illumination time. (C) Zoom-in plots of (B) with frame interval of 40.6 ms, showing that the scattering intensity of single Ag nanoparticles and background remains unchanged.

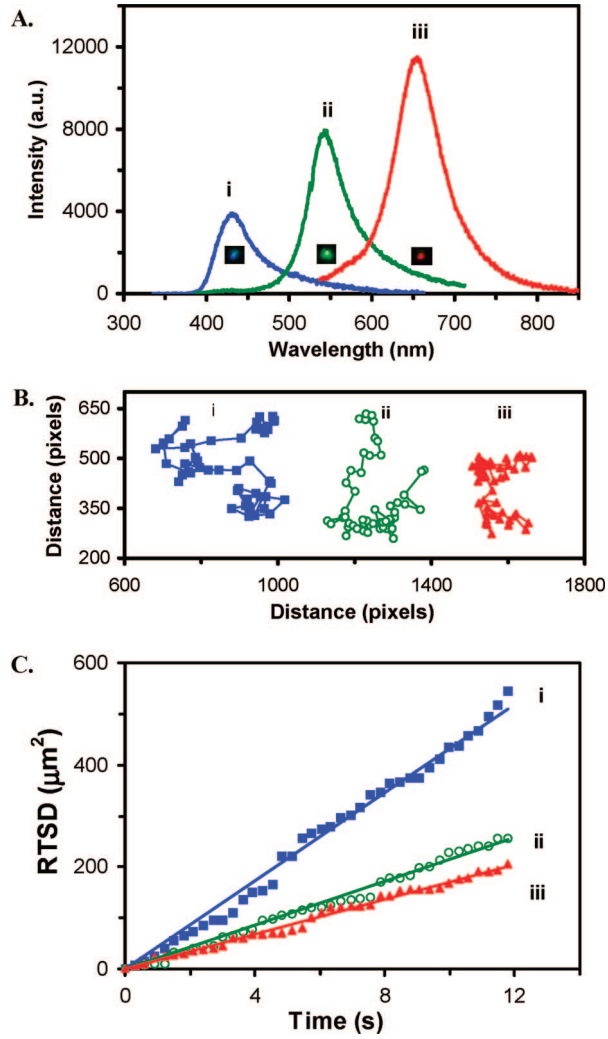

Figure 5. Real-time imaging and characterization of size-dependent diffusion of single Ag nanoparticles in solution. (A) Representative LSPR spectra of single Ag nanoparticles with a peak wavelength at 432, 543, and 655 nm. (B) Diffusion trajectories of single nanoparticles of (A) in solution. Each pixel = 0.067 μm. (C) Plots of RTSD of single nanoparticles in (B) *versus* diffusion time, for the (i) blue, (ii) green, and (iii) red nanoparticle, respectively.

low the size of nanoparticles to be directly determined in solution using their size-dependent LSPRS (color). LSPR spectrum of three representative colors (blue, green, and red) of single nanoparticles in Figure 5A shows the peak wavelength at 432, 543, and 655 nm, respectively.

Real-time diffusion trajectories of single nanoparticles recorded simultaneously in the solution using a CCD with an acquisition rate of 3.3 frames per second (fps) in Figure 5B show that the smallest nanoparticle (blue) travels the largest area while the largest nanoparticle (red) diffuses in the smallest zone. These results illustrate the dependence of the diffusion coefficient on the sizes (radii) of single nanoparticles, as described by the Stoke−Einstein equation, $D = kT/(6\pi\eta a)$, which states that the diffusion coefficient (D) depends on the viscosity of medium (η) and the radii (a) of solute (nanoparticle).[41,42] Thus, in order to simultaneously probe multiple nanoenvironments *in vivo* (*e.g.*, tracing intraembryonic fluids) in real time, it is essential to design and simultaneously detect monodisperse single nanoparticle probes *in vivo* in real time.

To track the diffusion of single nanoparticles in solution in real time, we used real-time square displacement (RTSD) (square of diffusion distance at a given time interval), instead of average (mean) of square displacement over time. Thus, as nanoparticles diffused, we were able to use RTSD to probe the gradient of viscosity of the medium in real time. This approach allowed us to probe the diffusion of single nanoparticles

in solution with millisecond temporal resolution in real time. Plots of RTSD *versus* diffusion time of the single nanoparticles in Figure 5C are linear, indicating that single nanoparticles diffuse by simple Brownian motion. The diffusion coefficient (D) of blue, green, and red nanoparticles, calculated by dividing the slope of a linear plot of RTSD *versus* time by 4 (note: RTSD $= 4D\Delta t$), is 10.42×10^{-8}, 5.23×10^{-8}, and 3.99×10^{-8} cm^2/s, respectively.

Simultaneous Imaging of Nanoenvironments of Segmentation-Stage Embryos. A representative optical image of a segmentation-stage zebrafish embryo in Figure 6A shows key components of embryo, including the inner mass of embryo (IME), the yolk sac (YS), the chorion space (CS), and the chorion layers (CHL) of the embryo. The zoom-in image of the area marked by the dashed square of Figure 6A shows the interface area of the chorion layers with egg water medium (extra-embryonic), the chorion space, and the interface area of the chorion space with the inner mass of the embryo (Figure 6B).

Segmentation stage of zebrafish embryos is a critical time in embryonic development during which the foundation and organization of the axial skeleton and the skeletal muscles of the vertebral column are being assembled.[43] Current studies show that each developing somite (vertebral segment) contains what will become two main tissue types, sclerotome and myotome, which give rise to the axial skeleton and skeletal muscle, for locomotion, respectively. Although it remains essentially unknown how somitogenic timing is regulated and how embryonic morphogenesis and cell migration are controlled,[44] genetic studies have demonstrated that certain signaling proteins exhibit critical functions in determining organization of embryonic asymmetrical pattern formation and organ placement in development. Note that diffusion and movements of motor proteins and signaling molecules highly depend on flow patterns and viscosity gradients of embryonic fluids. Thus, it is important to image flow patterns and viscosity gradients of embryonic fluids *in vivo* in real time while monitoring the development of embryos.

To this end, we simultaneously imaged and monitored the diffusion of three Ag nanoparticles with identical color (green) located in three representative areas of the chorion fluid of segmentation-stage zebrafish embryos, aiming to map flow patterns and viscosity gradients of embryonic fluids. As described in Methods, the low concentration of Ag nanoparticles (0.2 nM) was used to incubate with segmentation-stage embryos, and the diffusion measurements were completed in minutes. At such a low concentration and short exposure time, the effect of toxicity of Ag nanoparticles on the embryonic development is minimum as we illustrated previously.[6] We found that the diffusion trajectories of these identical nanoparticles are significantly different, as shown in Figure 6B. Note that single Ag

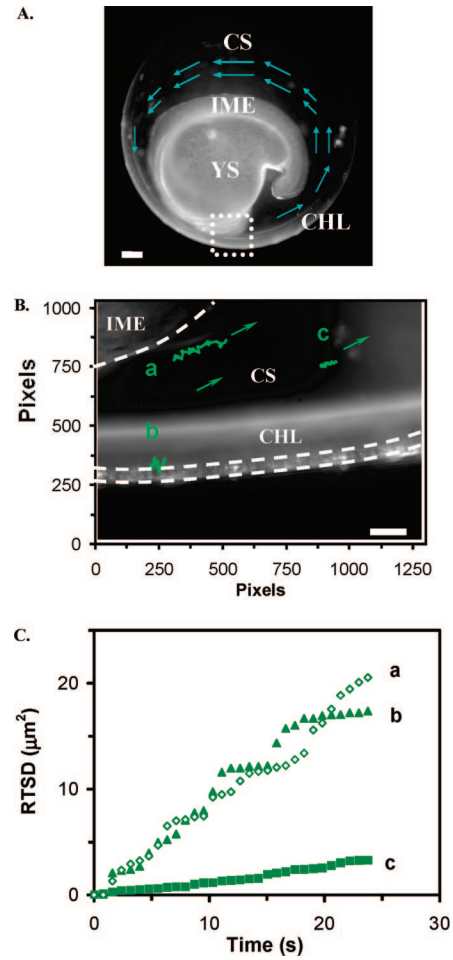

Figure 6. Real-time imaging and probing of nanoenvironments of a segmentation-stage (21 hpf) zebrafish living embryo. (A) An optical image of the living embryo shows the inner mass of embryo (IME), the yolk sac (YS), the chorion space (CS), and the chorion layers (CHL) of the embryo. The arrows show the counterclockwise flow patterns of embryonic fluid. (B) Zoom-in image of CS, region marked by a square in (A), shows a close-up of CS, and diffusion trajectories of three single green nanoparticles (a) at the interface of IME and CS, (b) at CHL, and (c) in the center of CS, show distinctive diffusion patterns, indicating different nanoenvironments of embryo. The arrows show the flow direction of nanoparticles and flow patterns of embryonic fluid. Each pixel = 0.067 μm. (C) Plots of RTSD of single green nanoparticles of (B) *versus* diffusion time show distinctive diffusion modes. Scale bar = 100 μm in (A) and 10 μm in (B).

nanoparticles with the identical color (LSPR) have similar size (radius), as illustrated in Figure 2D. The diffusion and trajectory analysis of three green Ag nanoparticles at varying distances from the embryonic cell surface exhibit the presence of counterclockwise flow patterns (Figure 6D) and a wide range of viscosity gradients of chorion fluid. The nanoparticles near the inner mass of embryos show the maximum linear displacement (Figure 6B,a), and the nanoparticles in the chorion space were the most restricted (Figure 6B,c). Overall, the nanoparticles were all moving in counterclockwise direction with flow rates ranging from 0.6 to 1.8 μm/s. Al-

though cilia-driven fluid flows have been observed in the zebrafish pronephros, brain and kupffer's vesicle,[27] to our knowledge, the counterclockwise flow patterns have not yet been reported in zebrafish chorion space.

We observed that the nanoparticles near the chorion layers (CHL), at the interface of intra- and extra-embryo, moved along the membrane and moved in and out of chorion pore canals (CPCs), showing a stepwise plot of RTSD *versus* diffusion time (Figure 6B and C,b). As the nanoparticles moved out of chorion pore canals, it exhibited simple Brownian motion with D of 2.2×10^{-9} cm^2/s. As the nanoparticles diffused into chorion pore canals, its diffusion patterns were restricted (steps in the plot), suggesting that the nanoparticle was trapped in the chorion pore canals, which altered their normal diffusion. Using the plot of RTSD *versus* time, we tracked the entry of individual nanoparticles into chorion pore canals and found that the period of time that individual nanoparticles stayed in the pores ranges from 0.1 to 15 s, which is consistent with what we observed previously.[6]

A similar phenomenon was observed for the nanoparticles diffusing at the interface of the chorion space and the inner mass of embryo (Figure 6B and C,a), showing a stepwise plot of RTSD *versus* time and illustrating that the nanoparticles exhibit Brownian diffusion with D of 2.3×10^{-9} cm^2/s. As the nanoparticles attempted to enter the inner mass of embryo, it displayed confined diffusion. Interestingly, the diffusion coefficient of nanoparticles near the inner mass of the embryo is similar to that near chorion layers, showing similar viscosity. Surprisingly, the nanoparticle near the center of the chorion space displays Brownian diffusion with the lowest diffusion coefficient of 2.8×10^{-10} cm^2/s (Figure 6B and C,c), showing the highest viscosity.

Using the same approach, we measured similar locations in two other embryos and found similar phenomena in that the nanoparticles near the center of the chorion space show the lower diffusion coefficient, ranging from 2.8×10^{-10} to 5.0×10^{-9} cm^2/s, and the higher diffusion coefficient in the chorion space near the inner mass of embryo, spanning from 2.3×10^{-9} to 1.1×10^{-8} cm^2/s. In the same segmentation-stage embryos, we observed stunningly high viscosity gradients (two orders of magnitude) of chorion space, with the highest viscosity around the center of chorion space and the lower viscosity in the area of chorion space that are either near the chorion layers or the inner mass of embryos.

The viscosity inside the embryo is ~20−188 times larger than the viscosity of the egg water, suggesting that the chorion layers are not porous enough to establish equilibrium of molecular (nanoparticle) transport. We also note that the slopes of plot of RTSD *versus* time in Figure 6C are not uniform through the entire measurements, indicating high non-uniformity of the chorion space and emphasizing the importance of probing these nanoenvironments in real time.

Taken together, the results showed that single nanoparticle photonics could serve as effective nanoprobes to simultaneously image and profile dynamics patterns and viscosity gradients of multiple nearby nanoenvironments of embryonic fluids *in vivo* at nanometer scale in real time. We found, for the first time to our knowledge, an interesting counterclockwise motion of the fluid flow in the chorionic space of the developing segmentation-stage zebrafish embryo. This is highly significant because recent studies have shown that fluid flow dynamics is of great importance and interest in the developing embryo for the establishment of the axial body and the positioning of the embryonic organ systems.[45] Even though many basic and interesting questions about mechanisms of embryonic body-plan dynamics and the formation of left−right asymmetry in vertebrates remain essentially unknown, studies have shown that fluid flow dynamics, specifically leftward counterclockwise fluid flow, is important in establishing left and right asymmetry in developing vertebrate organisms.[46–49] Flow dynamic patterns and viscosity gradients of embryonic fluids affect motion and diffusion modes of signaling molecules and cell migrations, which play key roles in controlling the division and differentiation of embryonic stem cells and embryonic morphogenesis.[48,49] Our findings will surely open up new inquiries about their roles in shaping embryonic morphogenesis. Further and substantial studies are underway to depict their roles in developing embryos.

SUMMARY

In summary, we have successfully synthesized Ag nanoparticles (11.3 ± 2.3 nm) and used a simple washing approach to reduce the ionic strength of the solution, which increased the thickness of the electric double layer on the surface of nanoparticles and thereby enhanced the surface ζ-potential of the nanoparticles. This approach allowed us to prepare optically uniform (75−99%) and purified Ag nanoparticles that are stable (not aggregated) in solution for months. Such superior stability enabled the effective use of Ag nanoparticles as individual nanoprobes for simultaneously imaging of multiple events at nanometer resolution *in vivo* and avoided time-consuming resynthesis and recharacterization process. These Ag nanoparticles resist photodecomposition and blinking and serve as single nanoparticle photonic probes for continuous and simultaneous imaging of multiple nanoenvironments of developing zebrafish embryos for hours. Unlike other particle tracking experiments, we determined given colored (sized) nanoparticles *in situ* using size-dependent LSPRS (colors) of single Ag nanoparticles and used the same color (size) of nanoparticles for simultaneously measuring viscosities and flow

patterns of multiple nanolocations of chorion space of segmentation-stage zebrafish embryos in real time. We found interesting counterclockwise flow patterns with rates ranging from 0.06 to 1.8 μm/s and astoundingly high viscosity gradients spanning two orders of magnitude in chorion space, with the highest viscosity observed around the center of chorion space and the lower viscosity at both interfacial areas near chorion layer and the inner mass of embryos. Work is in progress to further study the possible change of viscosity gradients and flow patterns of embryonic fluids over the entire development, aiming to better understand the correlation between embryonic fluid dynamics and embryonic stem cell differentiation and development of left−right asymmetry. One can now use the imaging tools developed in this study for simultaneously mapping of an array of dynamic events of interest *in vivo* at nanometer resolution in real time.

METHODS

Synthesis and Characterization of Stability of Ag Nanoparticles. Silver nanoparticles were synthesized by reducing $AgClO_4$ with $NaBH_4$ and sodium citrate as described in the following:[1,6] sodium citrate dihydrate (0.3 mM) and $NaBH_4$ (10 mM) were completely dissolved in 247.5 mL of ice-cold nanopure water. $AgClO_4$ (2.5 mL, 10 mM) was rapidly added to the reaction mixture, and the solution was homogeneously stirred at 425 rpm overnight at room temperature. After the reaction was completed, the solution was immediately filtered using 0.2 μm sterilized membrane filters (Whatman). Ag nanoparticles were immediately washed twice with nanopure water using centrifugation at 15 000 rcf (relative centrifugal force). The washed Ag nanoparticles were resuspended in nanopure water. Both washed and unwashed Ag nanoparticle solutions were stored in the dark at 4 °C for further characterization and used. The nanoparticle concentrations were calculated as described in our previous studies.[1,50] All reagents, such as $NaBH_4$ (>98%, EMD), sodium citrate (Sigma-Aldrich), and $AgClO_4$ (>99.9%, Alfa Aesar), were purchased and used without further purification. The nanopure water (Nanopore, 18 MΩ) was used to prepare solutions and rinse glassware.

The unwashed and washed Ag nanoparticles suspended in solution were characterized over 2 months after synthesis to investigate their stability using UV−vis spectroscopy (Hitachi U-2010), SNOMS, high-resolution transmission electron microscopy (HRTEM) (FEI Tecnai G2 F30 FEG, at 300 kV), and dynamic light scattering (DLS, Nicomp 380ZLS particle sizing system). The ζ-potentials of nanoparticles in solution were also measured using Nicomp 380ZLS particle sizing system.

SNOMS was well-described in our previous studies for real-time imaging and spectroscopic characterization of single nanoparticles in single living cells and for single molecule detection.[3,6,9,10,17,42,51,52] In this study, EMCCD (PhotonMAX) equipped with a spectrograph (SpectraPro-150) (Roper Scientific) was used for LSPR spectra characterization of single nanoparticles. EMCCD, a high-resolution CCD camera (Micromax, 5 MHz Interlin) (Roper Scientific), and color digital camera were used for imaging and characterization of single nanoparticles in solution and in embryos.

Characterization of Photostability of Single Nanoparticles. We determined the photostability of single Ag nanoparticles by acquiring sequential optical images of single Ag nanoparticles using a EMCCD camera with an exposure time at 100 ms and a readout time of 40.6 ms, while these nanoparticles were constantly irradiated under a dark-field microscope illuminator (100 W halogen) for 12 h, as described previously.[6] We measured the illumination power at the sample stage (focal plane of dark field), showing (0.070 ± 0.001) W during the experiment. We integrated scattering intensity of individual nanoparticles within a 20 × 20 pixel area (as marked by solid line squares in Figure 3A) and acquired average background intensity of several detection areas with the same size of detection volume (20 × 20 pixel) in the absence of nanoparticles (as marked by dashed line squares in Figure 3A). We subtracted the average background intensity from the integrated intensity of single nanoparticles and individual background area. We then plotted the subtracted integrated intensity of individual nanoparticles and background as a function of time (Figure 4B and C).

Breeding and Monitoring of Zebrafish Embryos. We housed wild-type adult zebrafish (Aquatic Ecosystems) in a stand-alone system (Aquatic Habitats), maintained, and bred zebrafish as described previously.[6,29] Typically, for breeding, two pairs of mature zebrafish were transferred into a clean 10 gallon breeding tank. The bottom of the tank was covered with marbles to prevent embryos from being consumed by zebrafish. A light (14 h)−dark (10 h) cycle was used to trigger breeding and fertilization of embryos and was maintained throughout the experiment. We collected the embryos at segmentation stage (21 hpf: 20−25 somites), transferred them into a Petri dish containing egg water (1.2 mM stock salts in DI water), washed twice with egg water to remove the surrounding debris, and placed them directly into a self-made microwell containing 0.2 nM Ag nanoparticles in DI water to image the diffusion of nanoparticles and probe nanoenvironments of the embryos in real time using our SNOMS. The diffusion measurements were completed within minutes.

Data Analysis and Statistics. We measured and analyzed at least 100 nanoparticles for characterization of size and color distribution of single nanoparticles using HRTEM and SNOMS, respectively. Each experiment was repeated at least three times. Thus, at least 300 nanoparticles were analyzed to gain sufficient statistics for determination of size distribution and color distribution of single nanoparticles and correlation of sizes and colors of single nanoparticles. The size distribution of bulk nanoparticles in solution measured by DSL is the same as those measured at the single nanoparticle level by HRTEM, demonstrating that the histogram of size distribution (Figure 2D) indeed represents bulk measurements at single nanoparticle resolution.

For diffusion measurements, we simultaneously monitored at least three nanoparticles with the same color in three representative locations of interest in chorion space of embryos, and each measurement was repeated at least three times in three different embryos. All other experiments were repeated at least three times, and representative data were presented.

Acknowledgment. This work is supported in part by NSF (NIRT: BES 0507036) and NIH (R01 GM076440). K.J.L. and P.D.N. are grateful for the support of NSF-GRAS (BES 0541661) and Dominion Scholar Fellowship, respectively. We thank CharFac of U. of Minnesota (a NNIN site funded by NSF) for their assistance characterizing Ag nanoparticles using HRTEM.

REFERENCES AND NOTES

1. Huang, T.; Nallathamby, P. D.; Gillet, D.; Xu, X.-H. N. Design and Synthesis of Single-Nanoparticle Optical Biosensors for Imaging and Characterization of Single Receptor Molecules on Single Living Cells. *Anal. Chem.* **2007**, *79*, 7708–7718.
2. Xu, X.-H. N.; Patel, R. P. Nanoparticles for Live Cell Dynamics. In *Encyclopedia of Nanoscience and Nanotechnology*; Nalwa, H. S., Ed.; American Scientific Publishers: Stevenson Ranch, CA, 2004; Vol. 7, pp 189−192, and references therein.
3. Xu, X.-H. N.; Song, Y.; Nallathamby, P. D. Probing Membrane Transport of Single Live Cells Using Single Molecule Detection and Single Nanoparticle Assay. In *New*

Frontiers in Ultrasensitive Bioanalysis: Advanced Analytical Chemistry Applications in Nanobiotechnology, Single Molecule Detection, and Single Cell Analysis; Xu, X.-H. N., Ed.; Wiley: New York, 2007; pp 41−65, and references therein.
4. Haes, A. J.; Van Duyne, R. P. A Nanoscale Optical Biosensor: Sensitivity and Selectivity of an Approach Based on the Localized Surface Plasmon Resonance Spectroscopy of Triangular Silver Nanoparticles. *J. Am. Chem. Soc.* **2002**, *124*, 10596–10604.
5. Schultz, S.; Smith, D. R.; Mock, J. J.; Schultz, D. A. Single-Target Molecule Detection with Nonbleaching Multicolor Optical Immunolabels. *Proc. Natl. Acad. Sci. U.S.A.* **2000**, *97*, 996–1001.
6. Lee, K. J.; Nallathamby, P. D.; Browning, L. M.; Osgood, C. J.; Xu, X.-H. N. *In Vivo* Imaging of Transport and Biocompatibility of Single Silver Nanoparticles In Early Development of Zebrafish Embryos. *ACS Nano* **2007**, *1*, 133–143.
7. Tiwari, S. B.; Amiji, M. M. A Review of Nanocarrier-Based CNS Delivery Systems. *Curr. Drug Delivery* **2006**, *3*, 219–232.
8. Xu, X. H. N.; Patel, R. P. Imaging and Assembly of Nanoparticles in Biological Systems. In *Handbook of Nanostructured Biomaterials and Their Applications in Nanobiotechnology*; Nalwa, H. S., Ed.; American Scientific Publishers: Stevenson Ranch, CA, 2005; Vol. 1, pp 435−456, and references therein.
9. Xu, X.-H. N.; Brownlow, W. J.; Kyriacou, S. V.; Wan, Q.; Viola, J. J. Real-Time Probing of Membrane Transport in Living Microbial Cells Using Single Nanoparticle Optics and Living Cell Imaging. *Biochemistry* **2004**, *43*, 10400–10413.
10. Xu, X.-H. N.; Chen, J.; Jeffers, R. B.; Kyriacou, S. V. Direct Measurement of Sizes and Dynamics of Single Living Membrane Transporters Using Nano-Optics. *Nano Lett.* **2002**, *2*, 175–182.
11. Yamada, T.; Iwasaki, Y.; Tada, H.; Iwabuki, H.; Chuah, M. K.; VandenDriessche, T.; Fukuda, H.; Kondo, A.; Ueda, M.; Seno, M.; Tanizawa, K.; Kuroda, S. Nanoparticles for the Delivery of Genes and Drugs to Human Hepatocytes. *Nat. Biotechnol.* **2003**, *21*, 885–890.
12. Agrawal, A.; Sathe, T.; Nie, S., Nanoparticle Probes for Ultrasensitive Biological Detection and Imaging. In *New Frontiers in Ultrasensitive Bioanalysis: Advanced Analytical Chemistry Applications in Nanobiotechnology, Single Molecule Detection, and Single Cell Analysis*; Xu, X.-H. N., Ed.; Wiley: New York, 2007; pp 71−89, and references therein.
13. Gao, X.; Cui, Y.; Levenson, R. M.; Chung, L. W.; Nie, S. *In Vivo* Cancer Targeting and Imaging with Semiconductor Quantum Dots. *Nat. Biotechnol.* **2004**, *22*, 969–976.
14. Bohren, C. F.; Huffman, D. R. Absorption and Scattering of Light by Small Particles; Wiley: New York, 1983; pp 287−380, and references therein.
15. KreibigU. VollmeM. *Optical Properties of Metal Clusters*; Springer: Berlin, 1995; pp 14−123.
16. Mie, G. Beiträg zur Optik Trüber Medien, Speziell Kolloidaler Metrallösungen. *Ann. Phys.* **1908**, *25*, 377–445.
17. Kyriacou, S.; Brownlow, W.; Xu, X.-H. N. Nanoparticle Optics for Direct Observation of Functions of Antimicrobial Agents in Single Live Bacterial Cells. *Biochemistry* **2004**, *43*, 140–147.
18. Murthy, S.; Bigioni, T. P.; Wang, Z. L.; Khoury, J. T.; Whetten, R. L. Liquid-Phase Synthesis of Thiol-Derivatized Silver Nanocrystals. *Mater. Lett.* **1997**, *30*, 321–325.
19. Huang, T.; Murray, R. W. Luminescence of Tiopronin Monolayer-Protected Silver Clusters Changes to that of Gold Clusters upon Galvanic Core Metal Exchange. *J. Phys. Chem. B* **2003**, *107*, 7434–7440.
20. Jiang, X. C.; Zeng, Q. H.; Yu, A. B. Thiol-Frozen Shape Evolution of Triangular Silver Nanoplates. *Langmuir* **2007**, *23*, 2218–2223.
21. Lee, P. C.; Meisel, D. Adsorption and Surface-Enhanced Raman of Dyes on Silver and Gold Sols. *J. Phys. Chem.* **1982**, *86*, 3391–3395.
22. Li, X.; Zhang, J.; Xu, W.; Jia, H.; Wang, X.; Yang, B.; Zhao, B.; Li, B.; Ozaki, Y. Mercaptoacetic Acid-Capped Silver Nanoparticles Colloid: Formation, Morphology, and SERS Activity. *Langmuir* **2003**, *19*, 4285–4290.
23. Machulek Junior, A.; de Oliveira, H. P.; Gehlen, M. H. Preparation of Silver Nanoprisms Using Poly(*N*-Vinyl-2-Pyrrolidone) as a Colloid-Stabilizing Agent and the Effect of Silver Nanoparticles on the Photophysical Properties Of Cationic Dyes. *Photochem. Photobiol. Sci.* **2003**, *2*, 921–925.
24. den Hertog, J. Chemical Genetics: Drug Screens in Zebrafish. *Biosci. Rep.* **2005**, *25*, 289–297.
25. Kahn, P. Zebrafish Hit the Big Time. *Science* **1994**, *264*, 904–905.
26. Kari, G.; Rodeck, U.; Dicker, A. P. Zebrafish: An Emerging Model System for Human Disease and Drug Discovery. *Clin. Pharmacol. Ther.* **2007**, *82*, 70–80.
27. Kramer-Zucker, A. G.; Olale, F.; Haycraft, C. J.; Yoder, B. K.; Schier, A. F.; Drummond, I. A. Cilia-Driven Fluid Flow in the Zebrafish Pronephros, Brain and Kupffer's Vesicle is Required for Normal Organogenesis. *Development* **2005**, *132*, 1907–1921.
28. Teraoka, H.; Dong, W.; Hiraga, T. Zebrafish as a Novel Experimental Model for Developmental Toxicology. *Congenit. Anom. (Kyoto)* **2003**, *43*, 123–132.
29. Westerfield, M. The Zebrafish Book: A Guide for the Laboratory Use of Zebrafish; Rerio, D., Ed.; University of Oregon Press: Eugene, OR, 1993; Chapters 1−4, http://zfin.org/zf_info/zfbok/zfbk.html.
30. Zon, L. I.; Peterson, R. T. *In Vivo* Drug Discovery in the Zebrafish. *Nat. Rev. Drug Discovery* **2005**, *4*, 35–44.
31. Cohen, S.; Leshanski, L.; Itskovitz-Eldor, J. Tissue Engineering Using Human Embryonic Stem Cells. *Methods Enzymol.* **2006**, *420*, 303–315.
32. Kusumi, A.; Nakada, C.; Ritchie, K.; Murase, K.; Suzuki, K.; Murakoshi, H.; Kasai, R. S.; Kondo, J.; Fujiwara, T. Paradigm Shift of the Plasma Membrane Concept from the Two-Dimensional Continuum Fluid to the Partitioned Fluid: High-Speed Single-Molecule Tracking of Membrane Molecules. *Annu. Rev. Biophys. Biomol. Struct.* **2005**, *34*, 351–378, and references therein.
33. Schwartz, R. E.; Linehan, J. L.; Painschab, M. S.; Hu, W. S.; Verfaillie, C. M.; Kaufman, D. S. Defined Conditions for Development of Functional Hepatic Cells from Human Embryonic Stem Cells. *Stem Cells Dev.* **2005**, *14*, 643–655.
34. Daniels, B. R.; Masi, B. C.; Wirtz, D. Probing Single-Cell Micromechanics *In Vivo*: The Microrheology of *C. elegans* Developing Embryos. *Biophys. J.* **2006**, *90*, 4712–4719.
35. Metallo, C. M.; Mohr, J. C.; Detzel, C. J.; dePablo, J. J.; VanWie, B. J.; Palecek, S. P. Engineering the Stem Cell Microenvironment. *Biotechnol. Prog.* **2007**, *23*, 18–23.
36. Apgar, J.; Tseng, Y.; Fedorov, E.; Herwig, M. B.; Almo, S. C.; Wirtz, D. Multiple-Particle Tracking Measurements of Heterogeneities in Solutions of Actin Filaments and Actin Bundles. *Biophys. J.* **2000**, *79*, 1095–1106.
37. Jacobson, K.; Ishihara, A.; Inman, R. Lateral Diffusion of Proteins in Membranes. *Annu. Rev. Physiol.* **1987**, *49*, 163–175.
38. Kusumi, A.; Sako, Y. Compartmental Structure of the Plasma Membrane for Receptor Movements as Revealed by a Nanometer-Level Motion Analysis. *J. Cell Biol.* **1994**, *125*, 1251–1264.
39. Kusumi, A.; Sako, Y.; Yamamoto, M. Confined Lateral Diffusion of Membrane Receptors as Studied by Single Particle Tracking (Nanovid Microscopy). Effects of Calcium-Induced Differentiation in Cultured Epithelial Cells. *Biophys. J.* **1993**, *65*, 2021–2040.
40. Wiley, B.; Sun, Y.; Xia, Y. Synthesis of Silver Nanostructures with Controlled Shapes and Properties. *Acc. Chem. Res.* **2007**, *40*, 1067–1076, and references therein.
41. Tinoco, I.; Sauer, K.; Wang, J.; Puglisi, J. D., Molecular Motion and Transport Properties. In *Physical Chemistry—Principles and Applications in Biological Sciences*; Prentice Hall: New York, 2002; pp 274−290.

42. Xu, X.-H. N.; Jeffers, R. B.; Gao, J.; Logan, B. Novel Solution-Phase Immunoassays for Molecular Analysis of Tumor Markers. *Analyst* **2001**, *126*, 1285–1292.
43. Stickney, H. L.; Barresi, M. J. F.; Devoto, S. H. Somite Development in Zebrafish. *Dev. Dyn.* **2000**, *219*, 287–303.
44. Luckenbill-edds, L. Introduction: Research News in Developmental Biology in 1895 and 1995. *Am. Zoo.* **1997**, *37*, 213–219.
45. Hirokawa, N.; Tanaka, Y.; Okada, Y.; Takeda, S. Nodal Flow and the Generation of Left−Right Asymmetry. *Cell* **2006**, *125*, 33–45, and references therein.
46. Nonaka, S.; Tanaka, Y.; Okada, Y.; Takeda, S.; Harada, A.; Kanai, Y.; Kido, M.; Hirokawa, N. Randomization of Left−Right Asymmetry due to Loss of Nodal Cilia Generating Leftward Flow of Extraembryonic Fluid in Mice Lacking KIF3B Motor Protein. *Cell* **1998**, *95*, 829–837.
47. Lbanez-Tallon, I.; Heintz, N.; Omran, H. To Beat or Not To Beat: Roles of Cilia in Development and Disease. *Hum. Mol. Genet.* **2003**, *12*, R27–R35, and references therein.
48. Levin, M. Left−Right Asymmetry in Embryonic Development: A Comprehensive Review. *Mech. Dev.* **2005**, *122*, 3–25, and references therein.
49. Hamada, H.; Meno, C.; Watanabe, D.; Saijoh, Y. Establishment of Vertebrate Left−Right Asymmetry. *Nat. Rev. Genet.* **2002**, *3*, 103–113, and references therein.
50. Xu, X.-H. N.; Huang, S.; Brownlow, W.; Salatia, K.; Jeffers, R. Size and Temperature Dependence of Surface Plasmon Absorption of Gold Nanoparticles Induced by Tris(2,2′-Bipyridine)Ruthenium(II). *J. Phys. Chem. B* **2004**, *108*, 15543–15551.
51. Kyriacou, S. V.; Nowak, M. E.; Brownlow, W. J.; Xu, X.-H. N. Single Live Cell Imaging for Real-Time Monitoring of Resistance Mechanism in *Pseudomonas aeruginosa*. *J. Biomed. Opt.* **2002**, *7*, 576–586.
52. Xu, X.-H. N.; Brownlow, W. J.; Huang, S.; Chen, J. Real-Time Measurements of Single Membrane Pump Efficiency of Single Living *Pseudomonas aeruginosa* Cells Using Fluorescence Microscopy and Spectroscopy. *Biochem. Biophys. Res. Commun.* **2003**, *305*, 79–86.